Adaptive Grid Radiation Hydrodynamics with TITAN

M. Gehmeyr [1] and D. Mihalas [2]

Laboratory for Computational Astrophysics

Astronomy Department, University of Illinois at Urbana-Champaign, 1002 W Green St., Urbana, IL 61801

and

National Center for Supercomputer Applications, Beckman Institute, 405 N Mathews, Urbana, IL 61801

Abstract: We have developed a code which solves the coupled sets of radiation transfer and fluid dynamics equations (time dependent in one spatial dimension) by employing a fully implicit adaptive grid procedure to detect, resolve, and track the relevant physical structures.

We have formulated TITAN as a general purpose code, written in a user friendly manner, and documented in detail. We intend to make this code available to the astrophysical community for the application to a broad variety of computational problems.

We demonstrate the code's power and versatility in a series of simple problems. They range from pure hydrodynamics test (shock tubes and blast waves), via radiation transfer test (radiative heating and cooling), to radiation hydrodynamics tests (radiative shocks and blast waves). These can be viewed as predecessors to a host of interesting astrophysical problems such as nova and supernova explosions and light curves, accretion onto compact objects, star formation, and stellar variability.

KEY WORDS: Radiation Hydrodynamics; Implicit Adaptive Grid; Noh's Shock Tube; Sub-

and Supercritical Shock; Radiative Blast

1. Introduction

We have written the implicit adaptive grid code TITAN which solves the comoving-frame equations of Newtonian radiation hydrodynamics in one spatial dimension. This code is designed as a general purpose code which addresses problems of astrophysical interest where the coupling of the radiation field with the fluid flow dominates the structure and evolution of the object under consideration.

One of the major difficulties of standard numerical methods is to resolve and to keep track of the nonlinear features of the system. They typically appear in spatially very narrow regions and introduce multiple length and time scales. In order to compute the dynamics of the system properly one therefore needs to resolve the energetics carefully.

We have implemented an implicit adaptive grid scheme to resolve and track the nonlinear features, such as shock waves, ionization fronts, or radiation fronts. In §2 we briefly review the physics of radiation hydrodynamics and the accompaning constitutive relations. In §3 we summarize some numerical details, especially the adaptive grid method, of the code and comment on the coding style. In §4 we discuss eight test problems: Noh's shock tube, Woodward's blast wave, Sedov-Taylor self-similar blast wave; radiative heating and cooling for different ratios of absorptive to scattering opacity and various transfer schemes; subcritical and supercritical shock waves, and a radiative blast wave in a power law atmosphere.

[1] mgehmeyr@deneb.astro.uiuc.edu

[2] dmihalas@altair.astro.uiuc.edu

2. The Mathematical Formulation

2.1. The Equations of Radiation Hydrodynamics

Following the textbook of Mihalas & Mihalas [7] we have formulated the equations of Newtonian grey radiation hydrodynamics for a single fluid in the comoving-frame of reference taking into account terms of $O\left(\frac{v}{c}\right)$. The two meaningful geometries for the radiation transfer are slab symmetry, designated by the parameter $\mu = 0$, and spherical symmetry, $\mu = 2$. The hydrodynamical equations by themselves can also be solved in cylindrical symmetry, $\mu = 1$.

Assuming that the mass within a shell of radius r (a slab of distance r) is described by the density:

$$m(r) = \int^{r} \rho(x) \frac{d(x^{\mu+1})}{\mu+1} \tag{1}$$

the set of governing equations are, defining the comoving time derivative as $D_t \equiv \frac{\partial}{\partial t} + u\frac{\partial}{\partial r}$:

continuity

$$D_t(\rho) + \rho \frac{\partial(r^\mu u)}{r^\mu \partial r} = 0 \tag{2}$$

momentum

$$\rho D_t(u) + \frac{\partial(p)}{\partial r} + \frac{\partial\left(r^{3\mu/2} P_Q\right)}{r^{\mu/2}\partial r} + \rho\left[\left(1 - \frac{\mu}{2}\right)g + 2\pi\mu\frac{Gm}{r^\mu}\right] - \frac{1}{c}\rho\chi_F F = 0 \tag{3}$$

radiative momentum

$$\rho D_t\left(\frac{F}{\rho c^2}\right) + \left[\frac{\partial(P)}{\partial r} + \frac{\mu}{2}\frac{(3P - E)}{r}\right] + \frac{F}{c^2}\frac{\partial u}{\partial r} + \frac{1}{c}\rho\chi_F F = 0 \tag{4}$$

fluid plus radiative energy

$$\rho D_t\left(e + \frac{E}{\rho}\right) + \frac{\partial(r^\mu F)}{r^\mu \partial r} + (p + P)\frac{\partial(r^\mu u)}{r^\mu \partial r} + P_Q\left[\frac{\partial u}{\partial r} - \frac{\mu}{2}\frac{u}{r}\right]$$

$$+\frac{\mu}{2}(E - 3P)\frac{u}{r} = 0 \tag{5}$$

radiative energy

$$\rho D_t\Big(\frac{E}{\rho}\Big) + \frac{\partial(r^\mu F)}{r^\mu \partial r} + P\frac{\partial(r^\mu u)}{r^\mu \partial r} + \frac{\mu}{2}(E-3P)\frac{u}{r}$$

$$+c\rho\Big[\kappa_E E - \kappa_P a_r T^4\Big] = 0 \tag{6}$$

In equation (5) e, the specific internal energy, and the radiative energy E are combined to form a "total internal" energy. Correspondingly there are two different contributions to the work: that of the gas pressure p and that of the radiative stress $P\frac{\partial(r^\mu u)}{r^\mu \partial r} + \frac{\mu}{2}(E-3P)\frac{u}{r}$. In addition we already provide for the work of an artificial stress P_Q. The energy is transported via the radiative flux F. We have neglected terms that combine radiation quantities with the gas acceleration.

The gas momentum equation (3) allows for gravitational forces in two geometries with G standing for the Newtonian gravitational constant and g for a constant acceleration. The radiation force, $\frac{1}{c}\rho\chi_F F$, the gradient of the gas pressure, and the artificial stress are exerted on the fluid elements, which move with velocity u.

The equation for the radiative flux (4) can be interpreted as the photon momentum equation which couples to the gas momentum via the last term.

The radiative energy equation (6) describes transport and work of the photons and constitutes, together with equation (4), the first two frequency and solid angle integrated moments of the transport equation. The last term in (6) can be viewed approximately as $\frac{1}{\tau_r}\Big(E - a_r T^4\Big)$, a_r denoting the radiation constant, and then be interpreted as a heat exchange on a time scale $\tau_r \equiv \frac{1}{c\,\kappa\rho}$, which is the duration of a photon traveling a mean free path $\frac{1}{\kappa\rho}$ between two scattering or absorption events. If $E > a_r T^4$ then the radiative energy is converted into heat, and *vice versa.* By assuming such a form of the radiative coupling term we restrict ourselves to a radiating fluid in LTE.

We refer to (4) & (6) as the two-equation formulation of the radiative transport, or "full transport", and it is a correct description in all regimes for the one dimensional case. We recognize in particular the "diffusion regime" when (4) becomes equivalent to

$$F = -\frac{c}{3\rho\chi}\,\frac{\partial E}{\partial r}. \tag{7}$$

If we use (7) in equation (6) then we speak of non-equilibrium diffusion because $a_r T_r^4 \equiv E$ defines a radiative temperature field which is allowed to differ from the fluid temperature T. In the case that we impose the condition that $\kappa_E E = \kappa_P a_r T^4$, or lax $T_r = T$, we are dealing with equilibrium diffusion.

In spherical symmetry it is customary to define the luminosity as the surface brightness $\mathcal{L} = 4\pi r^2 F$ of a shell with radius r.

2.2. The Constitutive Relations

2.2.1. Fluid equation of state

We allow for arbitrary equations of state as functions of the density and gas temperature:

caloric $$e = e(\rho, T), \tag{8}$$

thermal $$p = p(\rho, T). \tag{9}$$

They can be given in form of tables or as analytical formulae. In the first case we employ monotonic bicubic hermite polynomials to perform the interpolations. Important thermodynamical properties for the fluid are derived through the Gibbs form $de(\rho, T) = Tds(\rho, T) + p(\rho, T)d(\frac{1}{\rho})$, where s denotes the specific entropy. Among those of particular interest is the adiabatic index $\gamma = \frac{\partial \ln p}{\partial \ln \rho}\Big|_s$.

For the purpose of our test problems we assume a perfect gas so that: $p = \frac{R}{\mu}\rho T$, with R standing for the universal gas constant and $\overline{\mu}$ for the mean molecular weight. Prescribing a constant adiabatic index γ then relates the gas pressure to the gas energy: $e = \frac{1}{(\gamma-1)}\frac{p}{\rho}$.

2.2.2. Radiative equation of state

We close the two-equation formalism for the radiative transport, equations (6) & (4), via the variable Eddington factor f_E. The radiative pressure P in this description is simply proportional to E:

$$P = f_E E. \tag{10}$$

In order to evaluate f_E we integrate the static transport equation for the radiative intensity as a function of the solid angle ϕ, $I(x = \cos\phi)$, using a ray tracing technique. The Eddington factor is then computed as the ratio of the second to the zeroth moment:

$$f_E = \frac{\int_{-1}^{+1} I(x)x^2 dx}{\int_{-1}^{+1} I(x)dx}. \tag{11}$$

At the boundaries of the radiation field we evaluate a corresponding factor, called g_E. f_E describes the geometric properties of the radiation field. For an isotropic intensity distribution, $I(\phi) = I_o$, we obtain $f_E = \frac{1}{3}$. This corresponds to the diffusion limit of the two-equation formalism. If the intensity distribution peaks along the line of sight, $I(\phi) \propto \cos^2\phi$, we get $f_E = \frac{3}{5} > \frac{1}{3}$. The stronger the intensity field is pointed along the line of sight the closer $f_E \rightarrow 1$. This corresponds to the free streaming limit of the two-equation formalism. On the other hand, if the intensity distribution peaks sideways, $I(\phi) \propto \sin^2\phi$, we find $f_E = \frac{3}{15} < \frac{1}{3}$. This situation is often found in radiating shock fronts.

2.2.3. Opacities

In general the frequency dependent opacity $\chi(\nu)$ is given by contributions from absorption, $\chi^a(\nu)$, and scattering, $\chi^s(\nu)$. The grey formulation of the radiation hydrodynamics equations introduces three different opacity means: the flux mean, the absorption (or energy) mean, and the Planck mean:

flux mean $$\chi_F = \int_0^\infty [\chi^a(\nu) + \chi^s(\nu)]\ \frac{F(\nu)}{F}\ d\nu. \tag{12}$$

absorption mean $$\kappa_E = \int_0^\infty \chi^a(\nu)\ \frac{E(\nu)}{E}\ d\nu. \tag{13}$$

Planck mean $$\kappa_P = \int_0^\infty \chi^a(\nu)\ \frac{B(\nu,T)}{\sigma T^4/\pi}\ d\nu. \tag{14}$$

The flux and the energy mean both depend on the spectral distribution of the radiation field, whereas the Planck mean is given by the local gas temperature and density via the Planck distribution B. The evaluation of the first two opacity means therefore can be carried out correctly only if one also computes the frequency dependent, *i.e.*, non-grey, radiation field. This is often done with a multigroup approach. For the moment we have restricted our code to the grey transport.

Defining the Rosseland mean opacity

$$\chi_{Ross}^{-1} = \int_0^\infty [\chi^a(\nu) + \chi^s(\nu)]^{-1} \, \frac{\partial B(\nu, T)/\partial T}{4\sigma T^3/\pi} \, d\nu, \tag{15}$$

one can show that in diffusion approximation it equals to the flux mean, *i.e.*, $\chi_F = \chi_{Ross}$. For the purpose of our test problems we assume a constant χ_{Ross}. In order to simulate the effects of a scattering or absorption dominated fluid we set both the energy mean and the Planck mean equal to a fraction $0 \leq \zeta \leq 1$ of the Rosseland mean, *i.e.*, $\kappa_E = \kappa_P = \zeta \chi_{Ross}$.

2.3. The Boundary Conditions

We have equipped TITAN with a broad variety of boundary conditions; these allow for everything other than very special-purpose boundaries. They naturally fall into two categories to describe the boundaries of the radiation field and those of the fluid. The inner and outer (left and right) boundary conditions obey similar laws; hence is suffices to give just the generic formulation.

2.3.1. Radiative boundary

In general the radiative boundary is described by the radiative energy remaining constant $\Delta E = 0$. We provide for the optically transmitting and reflecting case. The first is defined through a flux which is computed from the free streaming formula. In addition the flux is allowed to be modified by a constant intensity field $I^{\pm}$. The second case is given through a zero flux condition. Furthermore we have the possibility of imposing a time dependent net flux.

transmitting $$F = \pm c g_{E} E \mp (2g_{E} + 1)\pi I^{\pm}. \qquad (16)$$

reflecting flux $$F = 0. \qquad (17)$$

imposed flux $$F = \Phi(t). \qquad (18)$$

In equation (16) g_{E} is a surface Eddington factor connecting E to F.

2.3.2. Eulerian boundary

The Eulerian boundary is given by the fixed grid condition $\dot{r} = 0$. We allow for three different cases. The transmitting condition demands that temperature, density, and velocity all remain constant across the boundary. The zero flux condition necessitates that the temperature and density stay constant while the velocity vanishes. For the nonzero flux condition density and temperature can be functions of time.

transmitting $$\Delta T = 0 \;\; ; \; \Delta\rho = 0 \; ; \; \Delta u = 0. \qquad (19)$$

zero flux $$\Delta T = 0 \;\; ; \; \Delta\rho = 0 \; ; \; u = 0. \qquad (20)$$

nonzero flux $$T = \Theta(t) \; ; \; \rho = P(t) \; ; \; u = 0. \qquad (21)$$

2.3.3. Lagrangean boundary

The Lagrangean boundary is given by the fixed mass condition $\dot{m} = 0$. We allow for two different forcings. In the piston driven case a time dependent velocity is assumed to move the boundary. Otherwise we allow for a forcing through an external pressure.

external velocity $$u = U_{ext}(t). \qquad (22)$$

external pressure $$p = P_{ext}(t). \qquad (23)$$

In addition to the boundaries we need to provide for phantom zones so that the difference stencil stays well defined. These phantom zones have to be chosen to reflect the physical properties of the boundary conditions.

3. Some Numerical Details and Principles of Coding

3.1. A Very Brief Description of TITAN

We discretize the physical equations (1)-(5) with finite differences. The physical quantities are defined on a staggered mesh. This allows us to write down the spatial operators in a straightforward manner, although some attention must be paid to the advection terms. Here we have employed the second-order, upwind Van Leer advection scheme [8]. The temporal evolution is achieved with a simple formula to advance from the old to the new time level. As a consequence our variables are functions of the integer pair (k, n), *i.e.,* of zone number and time index. In the equations all quantities x, aside from the temporal operator, are defined in between the old and the new time step with the aid of the time centering parameter θ,

$$x_k = \theta x_k^{n+1} + (1-\theta) x_k^n \ . \tag{24}$$

The algorithm becomes fully implicit for $\theta = 1$ and assumes backward-Euler differencing for $\theta = \frac{1}{2}$. In general we adopt $\frac{1}{2} < \theta \leq 1$.

The physical equations are formulated in conservation form using a discrete volume scheme. We provide the initial solution of the fundamental quantities for this set of algebraic equations. Their linearization results in a block pentadiagonal matrix. This system is inverted by the Henyey scheme [5] and then the solution is advanced in time by Newton's method. The data on the new time level are said to be converged when the maximum of the relative change of the variables is less than a specified tolerance, typically 10^{-5}, and the number of iterations lies within a specified range, say 3 and 15. The new time step is evaluated by a nonlinear control which incorporates accuracy considerations such that the temporal change of the variables is less than a given limit, typically 10%.

3.2. The Adaptive Grid Equation

At the core of our code is the adaptive grid algorithm. This couples the physical equations with a grid equation nonlinearly in a twofold manner. One way is the transformation of the physical equations according to the adaptive mesh Reynolds transport theorem, *cf.* Winkler, Norman, & Mihalas [13]. This changes the equations to an arbitrary frame of reference which can be quite different for each zone number. One discussion of how this transformation is carried out can be found in [2]. The other way is the addition of the grid equation which has only numerical significance and which determines which frame of reference for each zone at every time index is chosen. It needs input from physical quantities in order to find the features one wishes to resolve.

We adopted the grid equation according to Dorfi & Drury [3]. Their basic idea is to balance the grid concentration

$$\mathcal{C}_k^n = \frac{\mathcal{X}(r_{k+1}^n, r_k^n)}{(r_{k+1}^n - r_k^n)} \tag{25}$$

with the resolution function

$$\mathcal{R}_k^n = \sqrt{1 + \left[\mathcal{C}_k^n\right]^2 \sum_j \left[\frac{f_{j\,k+1}^n - f_{j\,k}^n}{\mathcal{X}(f_{j\,k+1}^n, f_{j\,k}^n)}\right]^2} \tag{26}$$

of the problem under consideration. The latter measures the arc length of various physical quantities f_k^n which are typically the density, gas energy, radiative energy, or gas pressure.

Demanding the grid equation

$$\mathcal{C}_k^n \propto \mathcal{R}_k^n \tag{27}$$

under the constraint

$$\frac{\alpha}{\alpha+1} \le \frac{\mathcal{C}_{k+1}^n}{\mathcal{C}_k^n} \le \frac{\alpha+1}{\alpha} \tag{28}$$

with $\alpha > 1$ one forces the grid to distribute in such a way that steep features in the fluid are resolved while maintaining approximately the same number of zones within the unit arc length over the whole domain. The detailed derivation and formulation of the grid equation can be found in [3]. The function $\mathcal{X}$ renders the expressions in (14) & (15)

dimensionless and serves as a scaling factor. We define it in two different ways: linear scaling with $\mathcal{X}(x_{k+1}^n, x_k^n) = x_{scale}$ and logarithmic scaling with $\mathcal{X}(x_{k+1}^n, x_k^n) = (x_{k+1}^n + x_k^n)$.

The grid equation itself contains further a time scale τ which sets the time step below which the distribution of the zones remains frozen in.

In addition to the adaptive grid the user can choose a fixed grid in either the Lagrangean or the Eulerian frame of reference.

3.3. The Artificial Stress

An important computational tool in finite difference computations is the artificial stress. We apply a tensor formulation adapted from [10] which is symmetric and trace free:

$$P_Q = -\frac{4}{3}\rho\mu_Q\left[\frac{\partial u}{\partial r} - \frac{\mu}{2}\frac{u}{r}\right]. \tag{29}$$

The artificial viscosity is evaluated according to:

$$\mu_Q = C_q^1 \ell c_s - C_q^2 \ell^2 \min\left[0, \frac{\partial(r^\mu u)}{r^\mu \partial r}\right]. \tag{30}$$

It incorporates a linear term in the shock width ℓ proportional to the local sound speed and a quadratic term in ℓ proportional to the divergence of the velocity field. The latter is turned on only in compression regions. The shock width is given either by a constant $\ell = \ell_0$ or set proportional to the radius $\ell = \ell_1 \cdot r$. The artificial stress P_Q appears in the momentum equation (3) in form of a shear force and in the energy equation (5) in form of stress work that dissipates some heat and functions as a source of entropy generation.

In adaptive grid computation the artifical stress serves as a means to establish a well defined ceiling for the discretization errors of the finite difference scheme. For this reason the shock width ℓ can typically be taken considerably smaller than fixed grid algorithms demand. We often combine the constant scalings for the shock width, ℓ_0, and the grid resolution, R_{scale}, and similarly choose the radius dependent expressions $\ell_1 \cdot (r_k^n + r_{k+1}^n)$ and $\mathcal{X}(r_{k+1}^n, r_k^n) = (r_{k+1}^n + r_k^n)$ together. Because of this correspondence we can see that the shock width ℓ sets a scale for the concentration $\mathcal{C}$ that the adaptive grid must obtain to resolve the shock and hence defines the maximum resolution. This will be eluded further later on in the discussion of the test problems.

3.4. Principles of Coding

Comprehensible. Each subroutine of has been given a header which contains a brief description of the contents, a calling sequence for easier location within the code, and possibly some references. In the body we make good use of comment cards to break the computation into meaningful parts and to make references to corresponding sections in the code documentation for comparison purposes.

Versatile. One general guideline during the development phase was to keep functionality of the code operators separate from its arguments wherever is was meaningful. This applies in particular to the linear solution precedure into which the Jacobian matrices of any set of equations can be fed. Hence they were formulated in a modular fashion so that they could be replaced with any other set. In this regard our code becomes a general PDE solver for the 1-D case. Similarly we provide for a general interface for the constitutive relations so that their specific evaluation is left to the user. The modular formulation of the physics part also enables the user to adapt or extend the code to his/her particular problem of interest.

Portable. We have written TITAN in standard FORTRAN 77. This allows for an immediate compilation and execution on a host of workstations and mainframes.

4. Discussion of Test Problems

4.1. Hydrodynamical Test Problems

4.1.1. Noh's shock tube

In this shock tube problem a piston of constant speed $v = -1$ pushes a cold gas with $\gamma = \frac{5}{3}$ into the origin. Courant & Friedrichs [1] have discussed this problem qualitatively and showed that an instantaneous shock of infinite Mach number is generated. The shock speed turns out to be $\frac{1}{2}(\gamma - 1)|v| = \frac{1}{3}$. Noh [9] defined this problem as a challenging benchmark for hydrodynamics codes that can be run in cartesian, cylindrical, and spherical geometry. In addition, there are analytical formulae against which the numerical results can be tested. We follow Noh's examinations at time $t = 0.6$ before the shock collides with the piston.

We represent the computational domain with 100 grid points and employ the density, pressure and energy in logarithmic scaling as our grid parameters together with $\alpha = 1.5$ and $\tau = 10^{-8}$. We obtain solutions to the Noh problem in all three geometries. Let us first consider the planar case which we calculate with a fixed and the adaptive grid. The superiority of the adaptive grid is well established: since the shock is the only nonlinear feature in the flow it is resolved with some 60 zones. The time $t = 0.6$ is reached after 160 time steps while constraining the time step to $\leq 10^{-2}$. The adaptive grid is locked into the shock frame and thus the code evolved almost statically. In contrast to that the shock has to move from one grid point to the next in the Eulerian computation thus allowing the time step to only vary between 10^{-5} and 10^{-4} (note that this still orders of magnitudes larger than the practical CFL number!). This computation exhibits all the problems induced by the use of the artificial viscosity as discussed in [9]. The adaptive grid, however, overcomes these difficulties very early on ($t < 10^{-2}$).

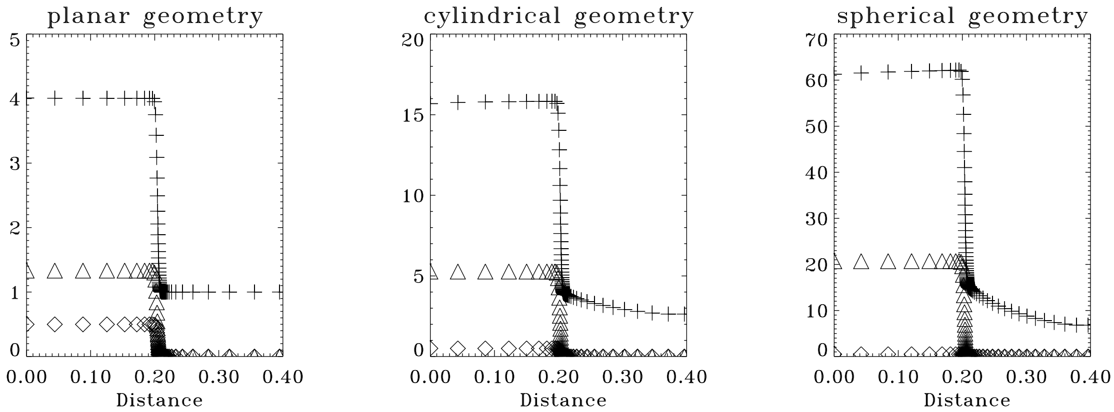

Fig. 1 (Noh's shock tube): density (+), energy (◇), and pressure (△) profiles in planar, cylindrical, and spherical geometry.

In figure 1 we plot profiles of the density, pressure, and energy at time $t = 0.6$ for planar, cylindrical, and spherical geometry. The adaptive grid behaves very similar in all cases producing sharp steps at the shock front. The step in energy is always $\frac{1}{2}$ because of the isothermal nature of the shock. The step in density equals to $3 \cdot 4^{\mu}$. The density profiles in the unshocked regions satisfy the analytical relations: $\rho(r,t) = (1 + t/r)^{\mu}$ which are valid for $t < \frac{3}{4}$ and $r > \frac{1}{3}t$. In the shocked regions the density plateau at $\rho(r,t) = 4^{\mu+1}$ for $0 \leq r \leq \frac{1}{3}t$ is well maintained in planar geometry and closely established in cylindrical and spherical geometry. We have evaluated the relative errors and found them to be between one tenth of a and a few percent in all cases. Since the theoretical plateau rises rapidly with μ the error becomes most visible in spherical geometry. We would like to remind that fixed grid computations usually generate errors of order unity for this problem! Therefore their solutions do not resemble the correct answer. The adaptive grid allows, for the first time, to generate good numerical results with little computational effort.

Next we simulate two different kinds of blast waves, one in planar and the other in spherical geometry.

4.1.2. Woodward's interacting blast waves

First we repeat a planar problem of two interacting blast waves that was invented by Woodward and is described in [14]. The computational domain is divided into three sections with three different but constant pressure regimes in them. In the left part we have $P(0 \leq r \leq \frac{1}{10}) = 1000$, in the middle part $P(\frac{1}{10} < r < \frac{9}{10}) = 0$, and in the right part $P(\frac{9}{10} \leq r \leq 1) = 100$ with an ideal gas resting at unit density. The adiabatic index is $\gamma = 1.4$. The density is initially constant, $\rho = 1$, across the domain $0 \leq r \leq 1$. We adopt again the same grid parameters as before but this time run the code with 200 grid points. The artificial viscosity is kept linear at $\ell_o = 10^{-4}$.

The large pressure steps at both ends of the cylinder create two shocks which travel towards the middle. The graph to the right (figure 2) shows their density profiles at an early stage (+'s marking individual grid points). One can see that the left front is much stronger than the right one. Further, rarefaction waves begin to appear in form of the density dips, which connect to the unit density near the walls.

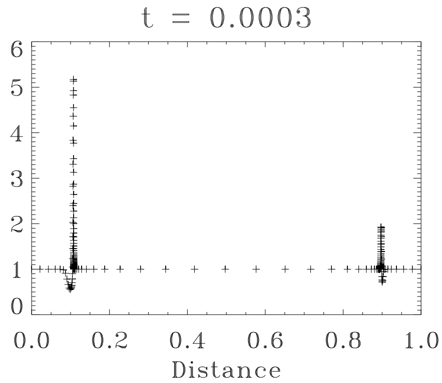

Fig. 2 (Woodward's blast waves): density profile at time t = 10^{-4}.

In the following figure, density profiles at four different times $t \in (1.57, 2.94, 3.85, 5.00) \times 10^{-2}$ are plotted. The top left graph shows the approach of the two shocks. Note in particular that the left one is much faster than the right one. The fast shock has a resolution of 10^5 and the slow shock one of several 10^4. The density between the shocks is still at the $\rho = 1$ plateau thus indicating that they move independently. The shocks are followed by contact discontinuities, both being resolved by 10^3. They connect to the rarefaction fans which stretch to the walls. The high resolution of the discontinuities leaves only a crude representation of the rarefaction fans with resolution of about 20. It is by choice that the adaptive grid is allowed to zone only into the shocks and has to neglect the rarefaction waves. At time $t = 0.028$ the shocks collide near position 0.69 and penetrate each other. When they separate a new third contact discontinuity forms in between them (lower right plot). At $t = 0.05$ the fast shock has reflected from the right wall but has not yet run into the third contact discontinuity.

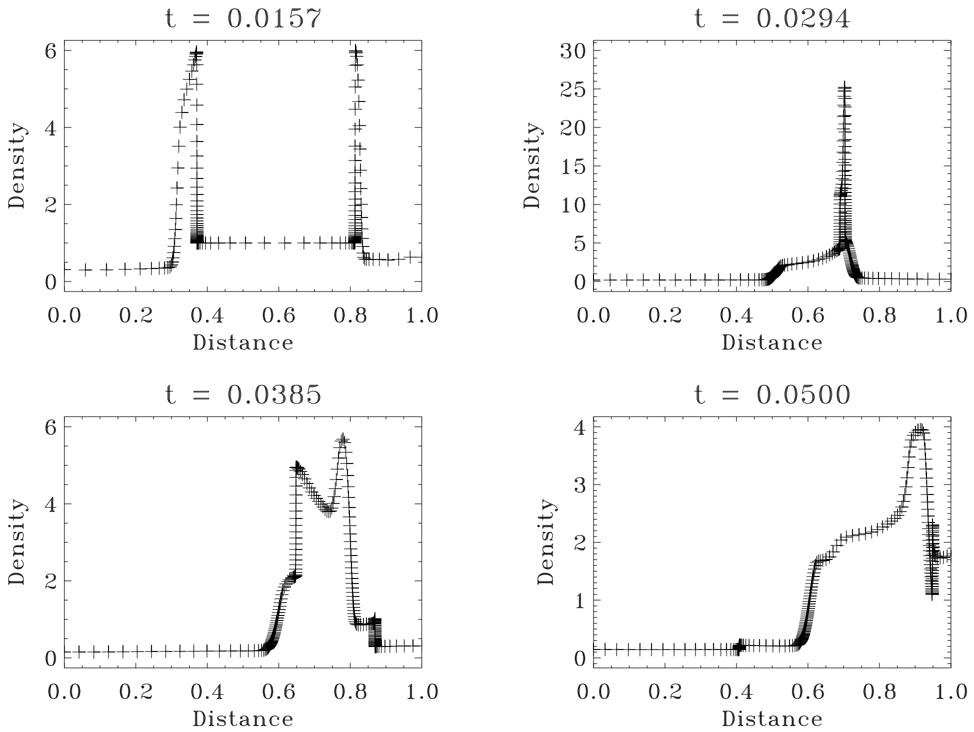

Fig. 3 (Woodward's blast waves): shock profiles at four different times (+'s indicate grid points).

A complete overview of the actions of all nonlinear waves can be obtained by investigating the space-time diagram of the density. The respective contours in logarithmic scale are drawn in figure 4. The shock fronts (due to their high resolutions) appear as thick lines, the contact discontinuities as broad lines, and the rarefaction waves as an ensemble of single contour lines.

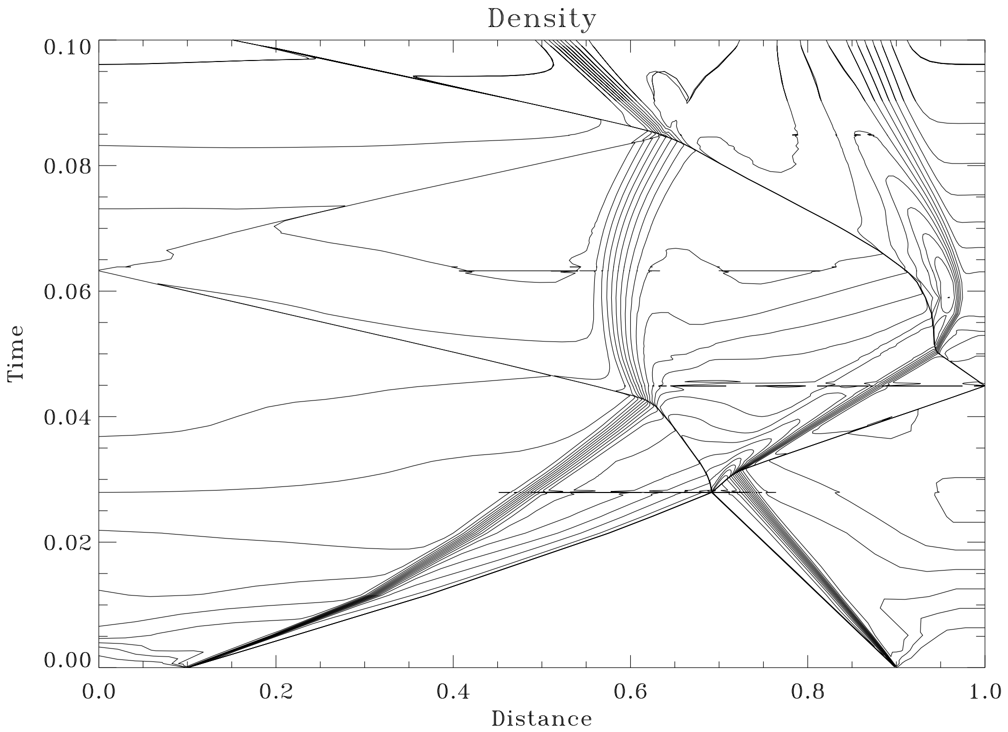

Fig. 4 (Woodward's blast waves): space-time diagram of the logarithmic density; 25 contour lines have been selected equidistantly.

The five density profiles (figures 2 & 3) are horizontal cross sections at the respective times. For times $t < 0.3$ there are the fast left traveling and slow right traveling shocks (speed given by the slope of the thick contour lines) each followed by a contact discontinuity which connects to a rarefaction fan. The fans are reflecting soon from the walls indicating that the region near the walls are being depleted quickly. At $t = 0.028$ the two shocks collide and slow down after the interaction while creating a secondary contact discontinuity. Shortly after the fast shock runs into the primary discontinuity from the right and accelerates again to near its original speed while the discontinuity is reflected. At $t = 0.045$ this shock reflects at the right wall and interacts with the discontinuity at about $t = 0.05$. Both nonlinear waves are slowed down considerably. The situation is comparable Sod's shock tube. New, however, is that the shock interacts with the secondary discontinuity and speeds up again. Shortly before $t = 0.045$ the slower right propagating shock collides with the other primary discontinuity and is greatly accelerated while the discontinuity is reflected. This shock now propagates uninterruptedly to the left wall. There it reflects at time $t = 0.063$ and moves with similar speed towards the right again until it runs again into the discontinuity. This time, however, the other shock front meets also with them leading to a multiple interaction of nonlinear waves.

A comparison of TITAN's computation with the original one by Woodward and Collela (using a special version of the PPMLR scheme on a domain of 3096 zones) tells that the shocks are well represented but the contact discontinuities lack sharpness. This can be accounted for in part to a fairly large artificial mass and energy diffusion which allowed our code to complete the run in a little over 1000 time steps (about a factor 5 less than the number of time steps PPMLR required). For comparison reasons the space-time diagram of the grid motion is presented in the following figure.

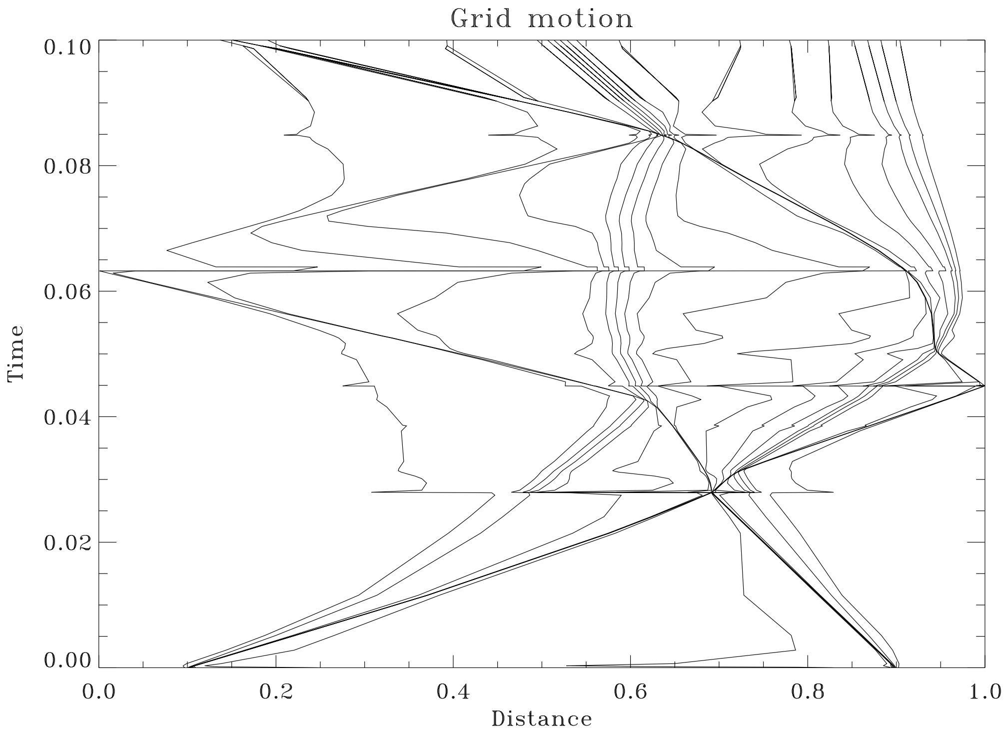

Fig. 5 (Woodward's blast waves): space-time diagram of the grid motion; the trajectory of every fourth zones is depicted.

Figure 5 demonstrates well that the adaptive grid keeps track of all discontinuities. Note the strong correlation between the grid motion and the density contours. Its typical behavior at the momentary absence of the shock(s) due to reflection from a wall or shock-shock interaction is also evident. In conclusion of this exercise we can highlight the generic behavior of the adaptive grid: Once the nonlinear features of the flow are resolved the adaptive grid locks into them and the code can evolve quasi-statically at time steps that are considerably larger than those of a fixed grid. When the grid needs to redistribute, as during the reflection of the shock from the wall or its interaction with the other shock or contact discontinuity, the time step drops by several orders of magnitude to accomplish this in a very short time interval.

4.1.3. Sedov-Taylor self-similar blast wave

We conclude our hydrodynamics benchmarking with the Sedov-Taylor blast wave. An energy deposition of 10^{50} $ergs$ at the center of a ball with radius $R_{max} = 10^9$ km generates a spherical shock that propagates in a self-similar fashion. The gas is assumed to have a polytropic index $\gamma = \frac{5}{3}$ and is initially at rest with a constant density of 10^{-8} g/cm^3 and temperature of 50 K. This time, density and pressure serve as the only grid parameters. Logarithmic scaling is choosen for all quantities involved. The grid α is again kept at 1.5, the shock width is $\ell_1 = 10^{-4}$ and we take 100 zones to cover the ball.

This problem is set up so that the shock wave reaches the surface of the ball after $t = 2 \times 10^5$ sec. The code completes the calculation in about 1000 time steps. The resolution of the shock front is about 10^6 during the evolution. In the figure to the right the evolution of this blast wave is illustrated. Snapshots of the density and the velocity at five different times $t \in$ (140, 2900, 26590, 93023, 197670) sec are overlayed. The upwind density is always 10^{-8} g/cm^3 with the material at rest. At the shock front the density jump remains constant 4×10^{-8} g/cm^3. The velocity jump decreases from 117 km/sec to 1.5 km/sec during these five instances. Both the density and the velocity profiles fall off to zero behind the shock.

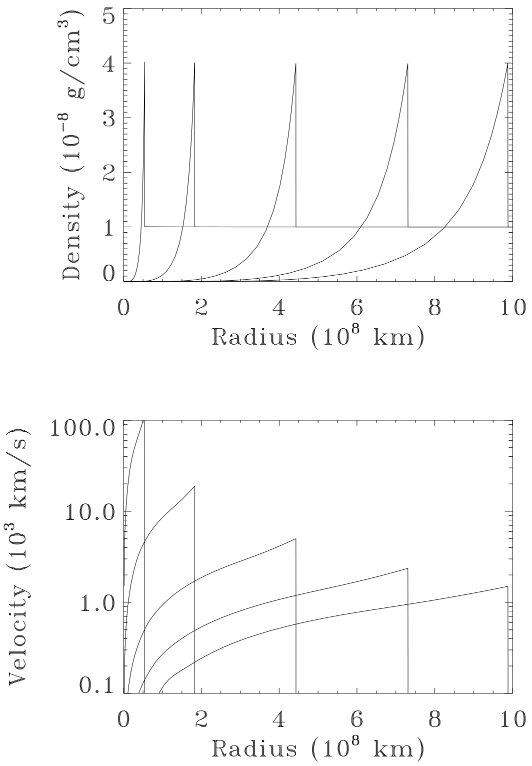

Fig. 6 (Sedov-Taylor blast wave): density and velocity profiles at five consecutive times.

The position, density, pressure, temperature, and velocity of the shock as a function of time are given in next figure. All variables vary strictly monotonically except for the shock density which remains at a steady value $\rho_s = 4 \times 10^{-8}\ g/cm^3$ as it should. In particular the expected relations

$$R_s(t) \propto t^{2/5} \tag{31}$$

$$v_s(t) \propto t^{-3/5} \tag{32}$$

$$T_s(t) \propto P_s(t) \propto t^{-6/5} \tag{33}$$

are satisfied. These are the analytical solution as discussed in the textbook of Landau & Lifshitz.

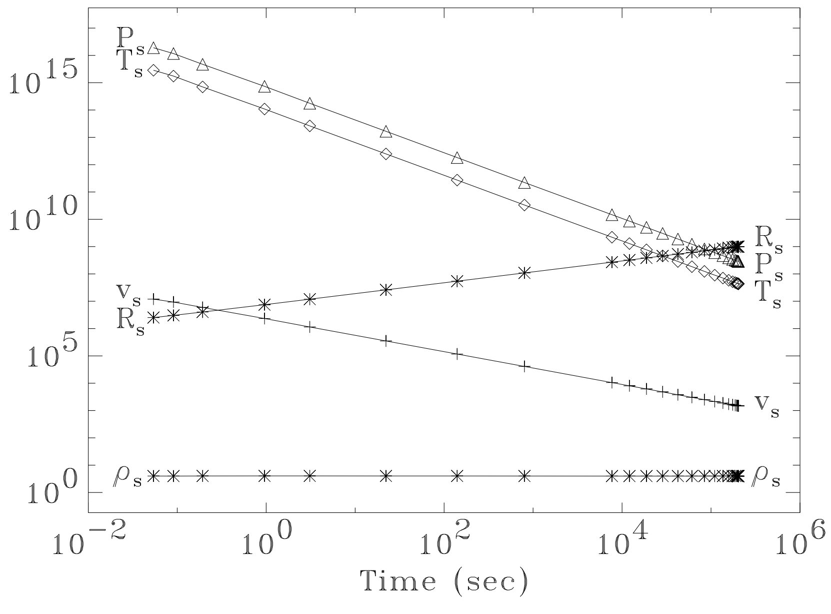

Fig. 7 (Sedov-Taylor blast wave): position R_s (km), density ρ_s (10^{-8} g/cm^3), temperature T_s (K), pressure P_s (dyn/cm^2), and speed v_s (km/sec) of the shock as a function of time; notice the power law dependencies.

The self-similarity of the computed flow is demonstrated in figure 8. It shows the profiles of density, pressure, and velocity in terms of the position, all measured with respect to the shock data. The graphics were generated by overlaying the actual grid values at six different times $t \in (140,\ 799,\ 12090,\ 42398,\ 110070,\ 174900)$ *sec.* One can verify that the shocked region obeys the analytical relations:

$$v/v_s \propto \ R/R_s \tag{34}$$

$$\rho/\rho_s \propto (R/R_s)^{3/(\gamma-1)} \tag{35}$$

and similarly for the pressure. Their functions jump to the preshock values and stay at a constant level. Compare this figure with the one in Landau & Lifshitz!

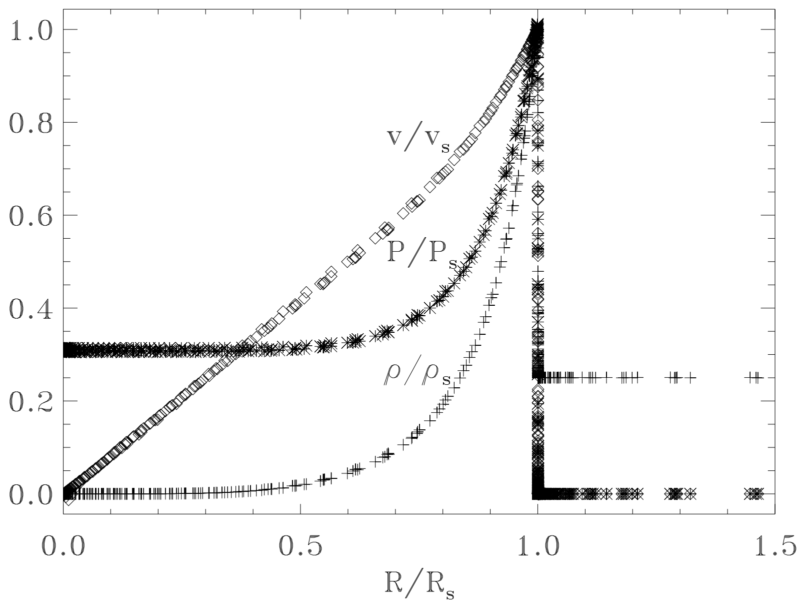

Fig. 8 (Sedov-Taylor blast wave): self-similarity in the profiles of the density ρ/ρ_s, pressure P/P_s, and velocity v/v_s generated through overlays from six different times $t \in (140,\ 532,\ 576,\ 1160,\ 2290,\ 4540)$ sec.

4.2. Radiation Test Problems

In this section we follow L. Ensman's suggestions for radiative tests [4]. We consider spheres of about 0.5 $M_\odot$ and radial extension of $R = 2.84 \times 10^3\ R_\odot$ that are filled with pure hydrogen at a constant density $\rho = 2.9677 \times 10^{-11}\ g/cm^3$. Further we assume the hydrogen to be fully ionized so that the opacity source are scattering electrons; hence we set the mean flux opacity proportional to the Thomson scattering opacity: $\rho\chi_F = \chi_e = 1.19 \times 10^{-11}\ cm^{-1}$. In addition we always equate the energy and Planck mean opacities, $\kappa_E = \kappa_P$, and allow them to differ from the mean flux opacity by a constant factor, $\kappa_E = \zeta\chi_F$, in order to illustrate the effects of a scattering versus absorption dominated gas.

4.2.1. Radiative heating tests

We set up this sphere to be in diffusion equilibrium at a luminosity $\mathcal{L} = 826\ \mathcal{L}_\odot$. From the available data one computes the radiative energy according to

$$E(r) = \frac{\mathcal{L}}{4\pi cR}\ \left[\sqrt{3} + 3\chi_e\Big(\frac{R}{r} - 1\Big)\right] \tag{36}$$

and from that the temperature profile via $T(r) = \sqrt[4]{E(r)/a_r}$. At time $t = 0$ we turn on a strong light source at the center with a $10^{1.5}$ times higher luminosity, $\mathcal{L}_c = 26,130\ \mathcal{L}_\odot$, which illuminates the gas sphere. The sphere now has to evolve into a new radiative equilibrium at this higher luminosity.

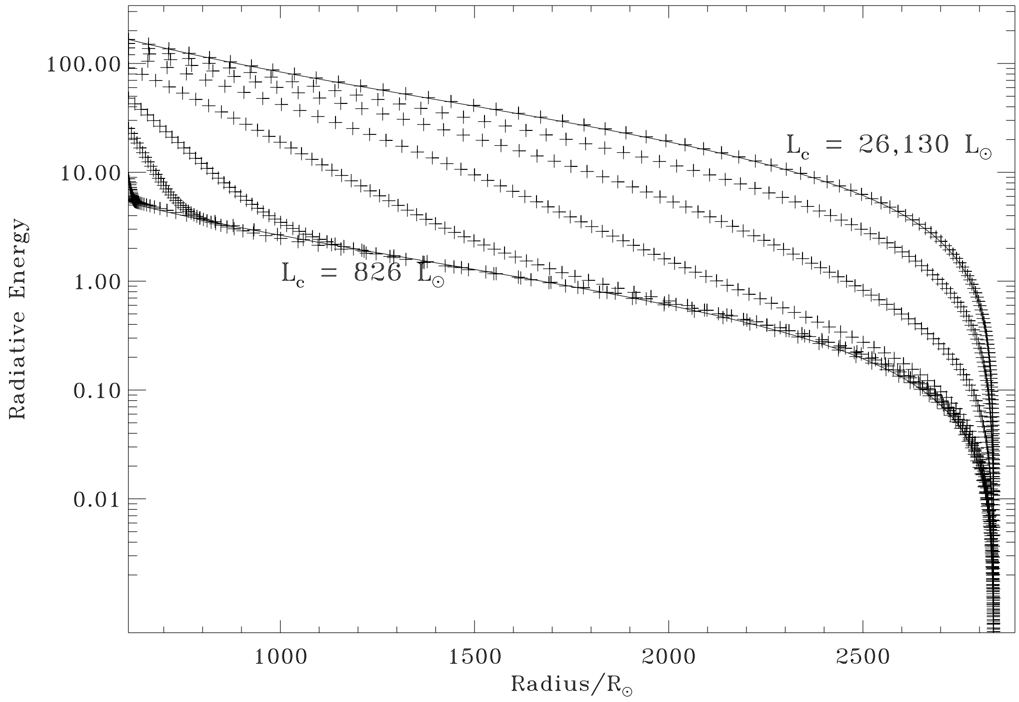

Fig. 9 (Heating towards radiative equilibrium): profiles of the radiant energy (+) at different times during the relaxation of a scattering dominated atmosphere with $\rho\kappa_P = 10^{-5}\ \chi_e$.

This graph illustrates how the higher central luminosity changes the profiles of the radiative energy in time. Initially the sphere is at equilibrium at the lower luminosity, $\mathcal{L}_c = 826\ \mathcal{L}_\odot$, which is represented by curve $E(r)$ at the bottom (+'s indicating individual grid points). This curve relaxes and the radiative energy increases until the new equilibrium at the higher luminosity, $\mathcal{L}_c = 26,130\ \mathcal{L}_\odot$, is reached. For both the initial and the final $E(r)$ curve the analytical solution from equation (36) were overlayed. The agreement between the analytical (assuming diffusion) and numerical (assuming variable Eddington factors) result is remarkable. This should be expected because the shell is optically thick except right underneath the surface and hence the diffusion regime is established everywhere else.

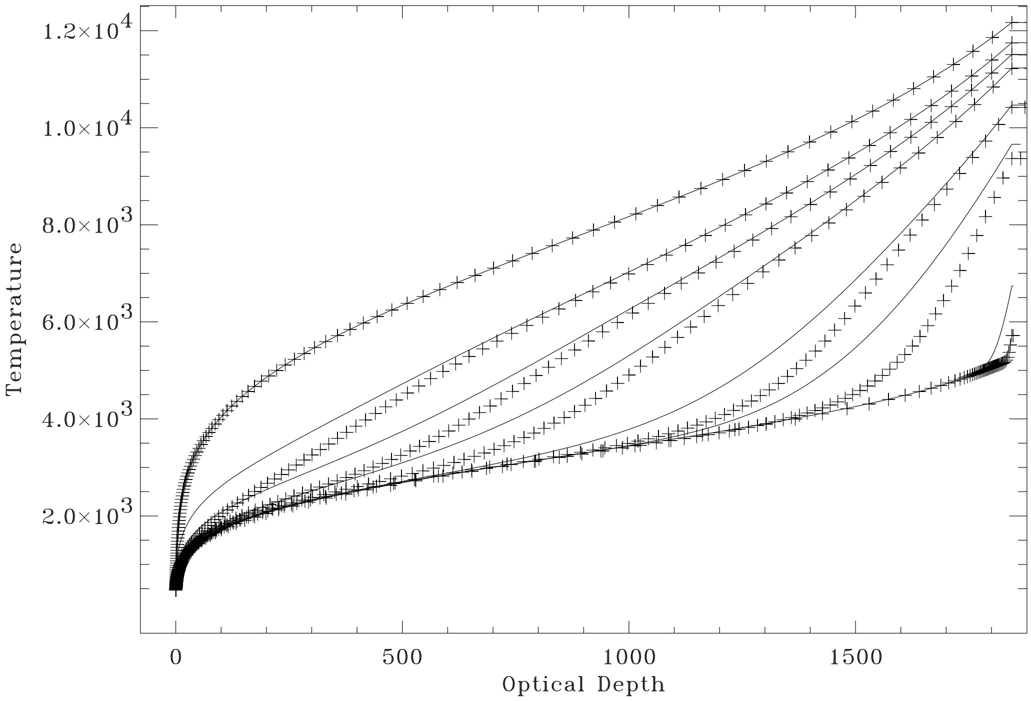

Fig. 10 (Heating towards radiative equilibrium): profiles of the gas (+) and radiation (—) temperature at different times during the relaxation of a scattering dominated atmosphere with $\rho\kappa_P = 10^{-5}\ \chi_e$.

The heating of the gas (+) and radiative (—) temperature by the central light source is given in figure 10. It shows the relaxation of their profiles as a function of the optical depth at various times. Both bottom curves are the initial condition in which the two temperatures agree because of equilibrium diffusion. When the light source is turned on a radiation wave moves through the sphere thereby heating up the gas. Since a weak coupling between the gas and the radiation field is assumed, $\zeta = 10^{-5}$, the gas temperature rises noticebly slower than the radiative temperature. As soon as the higher luminosity value has reached the surface both temperatures agree once again and the new radiative equilibrium is established. Because most of the gas is optically thick the diffusion regime prevails and the temperature follows again the profile from equation (36).

This experiment is repeated with different factors ζ. The sphere relaxes to the same equilibrium state every time. Figure 11 depicts the evolution of the surface luminosity for six different choices $0 \leq \zeta \leq 1$. The correspondence between the symbols and the ratios f_r for the gray opacity is as follows: $\zeta = 0$ ($\Box$), 10^{-9} ($\triangle$), 10^{-7} ($\diamond$), 10^{-5} ($*$), 10^{-2} ($+$), 1 (—). The relaxation of the temperature profiles from the previous figure is represented here by the asterisk. Note that the time the radiation wave takes to reach the surface and hence begins to raise the luminosity is, with- in a factor of 2, the same in all cases, namely around 6×10^6 *sec*. This number is in reasonable agreement with the classical diffusion time scale $\chi_e R^2/c \approx 1.4 \times 10^7$ *sec*. The spheres with almost pure scattering opacities reach the higher luminosity plateau first. Those spheres with almost pure absorptive opacities attain it later.

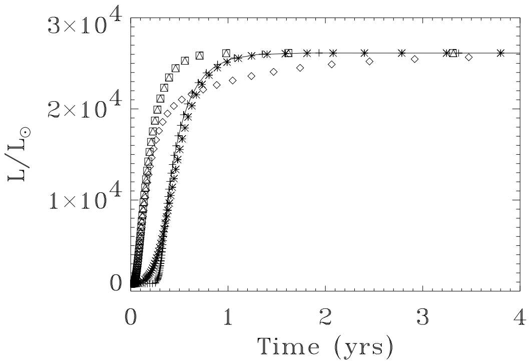

Fig. 11: Relaxation of the surface luminosity for six different opacities

The experimental setup allows us further to investigate the different radiative transport schemes in TITAN. There are three choices:

"equilibrium diffusion":

The gas and radiative temperature are not distinguished, $E = a_r T^4$, and the radiative flux is evaluated according to equation (7). The differentiation between the mean opacities becomes meaningless and only the total opacity is considered.

"non-equilibrium diffusion":

The radiative flux is still computed according to equation (7). But now the radiation energy E is computed from equation (6). Two temperatures are possible and the absorptive character of the gas can be taken into account. Both diffusion cases demand a constant Eddington factor $f_E = \frac{1}{3}$.

"full transport":

The radiation field is described by the two equations (4) & (6). Since they necessitate an estimate for f_E one obtains also information about the angular distribution of the intensity field.

The consistency of the three approaches can be checked in the context of the hydrogen spheres. The equilibrium diffusion computation can also be simulated with non-equilibrium diffusion by setting $\kappa_E = \chi_F$. Since the gas is optically thick (aside right underneath the surface) the corresponding full transport calculation should behave in the same manner. Performing the actual runs demonstrates a tight agreement between the three transport schemes.

We calculate the relaxation with the full transport scheme under the assumption that the absorptive opacity is considerably smaller than the total opacity: $\rho\kappa_E = 10^{-5}\ \rho\chi_F = 10^{-5}\ \chi_e$. This defines the case of a scattering dominated gas. The computation is carried out with our adaptive grid. This time we take the radiation energy and the luminosity as the grid parameters in logarithmic scaling and set $\alpha = 3$, $\tau = 10^3$.

4.2.2. Radiative cooling tests

We now take the equilibrium model described above as the initial condition. At $t = 0$ we turn the light source at the center off. This time we choose a fixed (Eulerian) grid instead of the adaptive grid and perform the runs with the full radiative transport scheme.

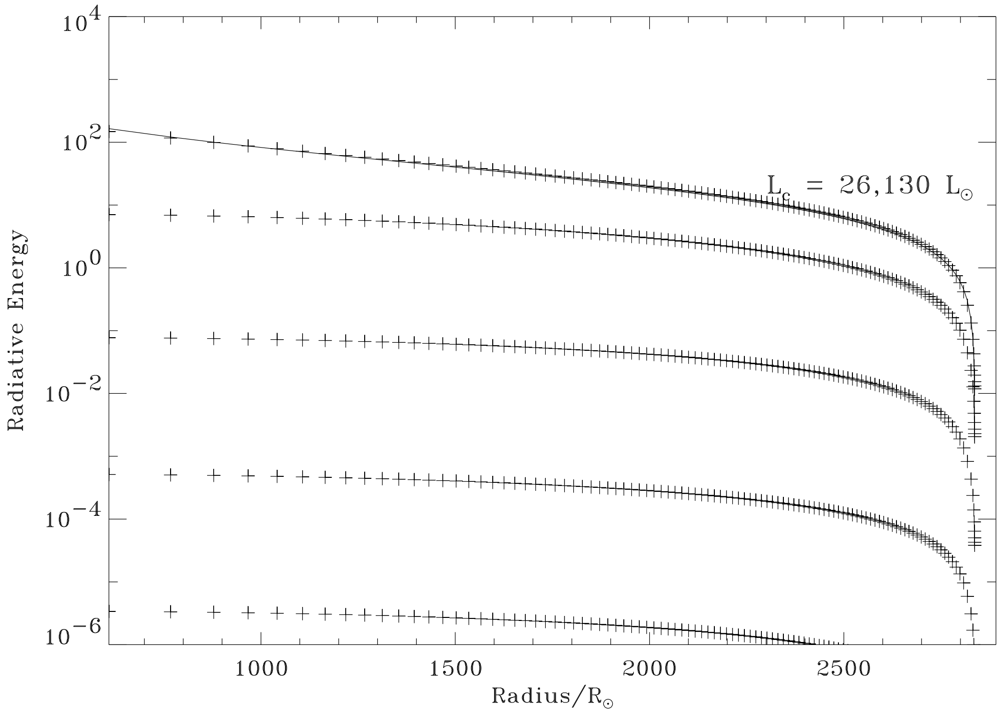

Fig. 12 (Cooling away from radiative equilibrium): profiles of the radiant energy (+) at different times during the relaxation of a scattering dominated atmosphere with $\rho\kappa_P = 10^{-7}\ \chi_e$.

This graph illustrates how the radiative energy decreases in time once the central luminosity is turned off. Initially the sphere is at equilibrium at $\mathcal{L}(0) = 26,130\ \mathcal{L}_\odot$ which is represented by the curve $E(r)$ (+'s again marking the grid points) at the top with the analytical solution overlayed. As time progresses, E decreases throughout the sphere as radiant energy leaks out, and the gradient of E flattens, consistent with $\mathcal{L}(t)$ deminishing to zero. At the surface a sharp gradient continues to drive $\mathcal{L}(t)$ outward. For $t \to \infty$ it goes to zero, $E \to 0$, which represents the new equilibrium when $\mathcal{L}_c = 0$.

Just like before one can consider different strengths of the gas-radiation coupling.

In figure 13 the decline of the surface luminosity for various gray opacities defined by the ratios $0 \leq \zeta \leq 1$ are plotted. Again these ratios correspond to the symbols in the following way: $\zeta = 0$ ($\square$), 10^{-9} ($\triangle$), 10^{-7} ($\diamond$), 10^{-5} ($*$), 10^{-2} ($+$), 1 (—). The curve of the diffusion regime ($\zeta = 1$) is representative of all regimes with $\zeta > 0$. Their analyses tells that the long time behavior

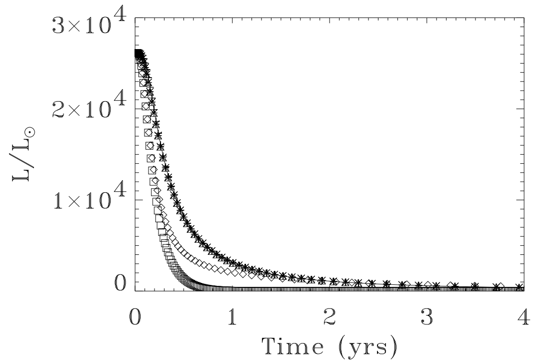

Fig. 13: Relaxation of the surface luminosity for six different opacties

the luminosity decay follows a power law, $\mathcal{L}(t) \propto t^{-s}$, with the power being close to $s = \frac{1}{3}$. In contrast to that the regime of complete decoupling between the gas and radiative temperature, $\zeta = 0$, is characterized by an exponential decay, $\mathcal{L}(t) \propto e^{-t/s}$, with the time scale $s \approx 1.7 \times 10^7$ *sec* being close to the classical diffusion time. This regime behaves differently because the cooling wave alters only the radiative temperature but leaves the profile of the gas temperature unchanged.

In figure 14 the profiles of the gas ($+$) and radiative (—) temperature for the case $\zeta = 10^{-7}$ are plotted. Initially they are in equilibrium but the decoupling begins immediately. One observes that the profile of the radiative temperature is merely shifted downward in time. Simultaneously the profile of the gas temperature is modified to become a constant. Since the bulk of the total opacity comes from electron scattering the radiation cools off faster than the gas so that the gas energy contribution to the luminosity rises soon to domination. Note that the radiative temperature is related to the radiative energy via equation (36) and therefore shows the same behaviour as E in figure 12.

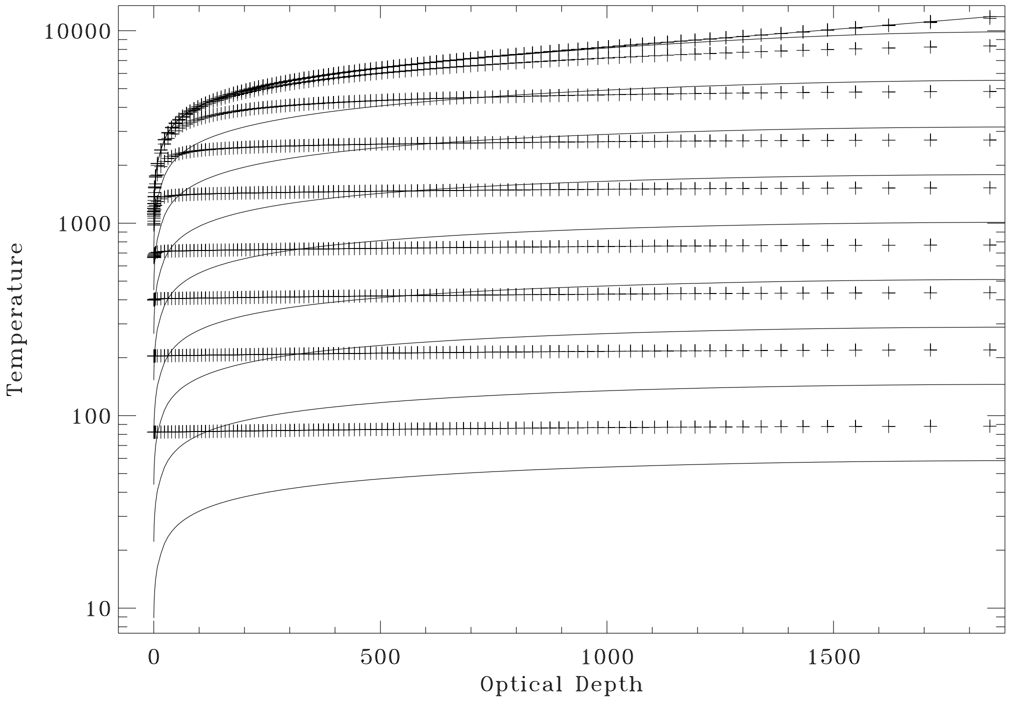

Fig. 14 (Cooling away from radiative equilibrium): profiles of the gas (+) and radiation (—) temperature at different times for a scattering dominated atmosphere with $\rho\kappa_P = 10^{-7}\ \chi_e$.

4.3. Radiation Hydrodynamics Test Problems

The fundamental understanding of radiating shocks was developed by Zel'dovich & Raizer and additional discussion of the phenomena involved is given by Mihalas & Mihalas. This section describes three radiation hydrodynamics benchmarks. All tests are carried out in spherical geometry. The full transport scheme for the radiative field is employed. We follow again L. Ensman's test setups.

We first consider a thin shell with an inner radius $R_i = 8 \times 10^6\ km$ and outer radius $R_o = 8.7 \times 10^6\ km$ filled with a cold gas at constant density $7.78 \times 10^{-10}\ g/cm^3$. Further, we assume a shallow temperature profile

$$T(r) = 10 + 75\ \frac{r - R_o}{R_i - R_o}\ K. \tag{37}$$

The Rosseland mean opacity is taken to be constant $\rho\chi_{Ross} = 3.115 \times 10^{-10}\ cm^{-1}$, and all of it is absorptive, $\zeta = 1$. The gas is initially at rest. At time $t = 0$ a piston at the inner radius is moved outwards at a constant high speed. A shock front is thus formed which couples strongly to the radiation field. If the maximum temperature immediately ahead of the shock is less than the downstream temperature one speaks of a "subcritical" shock, the case of equality one speaks of a "supercritical" shock.

In the following calculations we represent the sphere by 100 grid points. Density and mass in logarithmic scaling are selected as the sole grid parameters along with $\alpha = 1.5$ and $\tau = 10^{-20}$. The shock width is taken to be proprotional to the radius, $\ell_1 = 10^{-5}$, to demand a high resolution. All runs are executed fully implicit, *i.e.,* with time centering parameter $\theta = 1$.

4.3.1. Subcritical shock

The piston speed is 6 km/sec. Figure 15 shows the radiative shock front propagating towards the surface. The four quantities gas T and radiative temperature T_r, radiative flux F, and density ρ are plotted as functions of the radius at seven different times. The shock front is located where the flux is largest. The temperatures just ahead of the shock are always smaller than those in the shocked region thus defining this run as a subcritical shock.

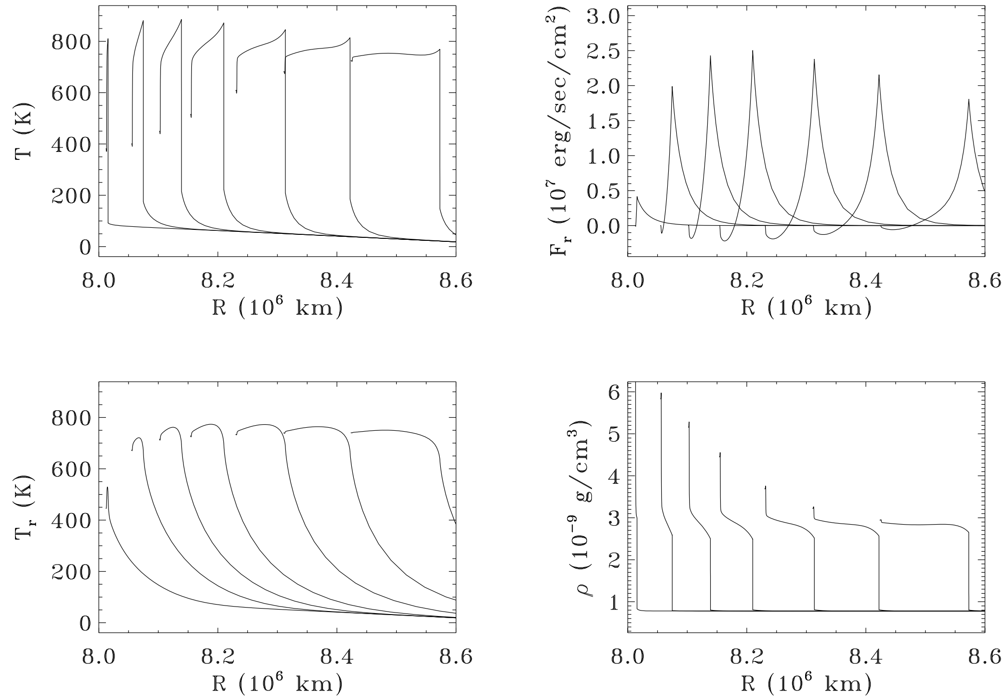

Fig. 15 (Subcritical shock): evolution of the gas and radiative temperature, the radiative flux, and the velocity profiles while a piston of speed 6 km/sec pushes the left boundary towards right.

It is often useful to look at the dependencies of the physical quantities on other coordinates. The following figures illustrate this for the example of the gas temperature. The same seven snapshots were taken but instead of showing them as a function of the radius they are now plotted as a

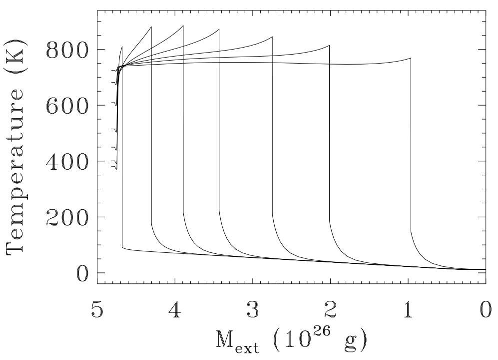

function of the exterior mass, of the optical depth, and of the grid point (zone index). The dependency $T = T(M_{ext})$ is the Lagrangean representation of the data which emphazises the outermost layers of the gas sphere. The graph $T = T(\tau)$ shows the temperature profile from a radiation transport perspective which stresses how transparent the features are. These functional dependencies help the physical interpretation of the results. On the other hand, the profile $T = \{T_k \; ; \; k = 1, \ldots, 100\}$ is interesting from a numerical point of view because one can learn from them how well the calculation was carried out. In the given example one can, for instance, see that the temperature jumps in the shock are well resolved by about 10 grid points.

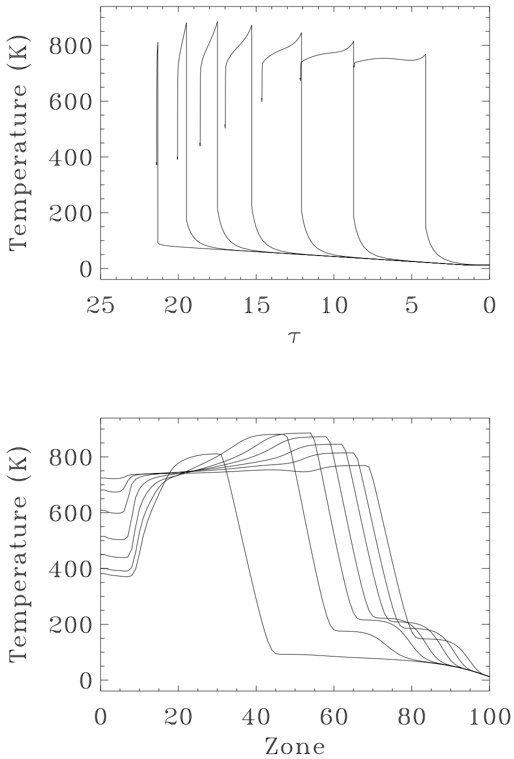

Fig. 16 (Subcritical shock): three different representations of the evolution of the temperature profile

Its characteristic features, as explained in Zel'dovich & Raizer, are an overshoot of the gas temperature, a nearly symmetric profile of the radiative flux, and an extended non-equilibrium region upstream from the shock, which is generated by the effects of radiative preheating from the flux. In figure 17 the density, gas and radiative temperature, flux and Eddington factor (scaled so that 1.0 corresponds tp $f_E = \frac{1}{3}$), and velocity are plotted in dependency on the optical depth away from the front, $(\tau - \tau_s)$, at the half piston crossing time ($t = 56,581$ sec to be exact).

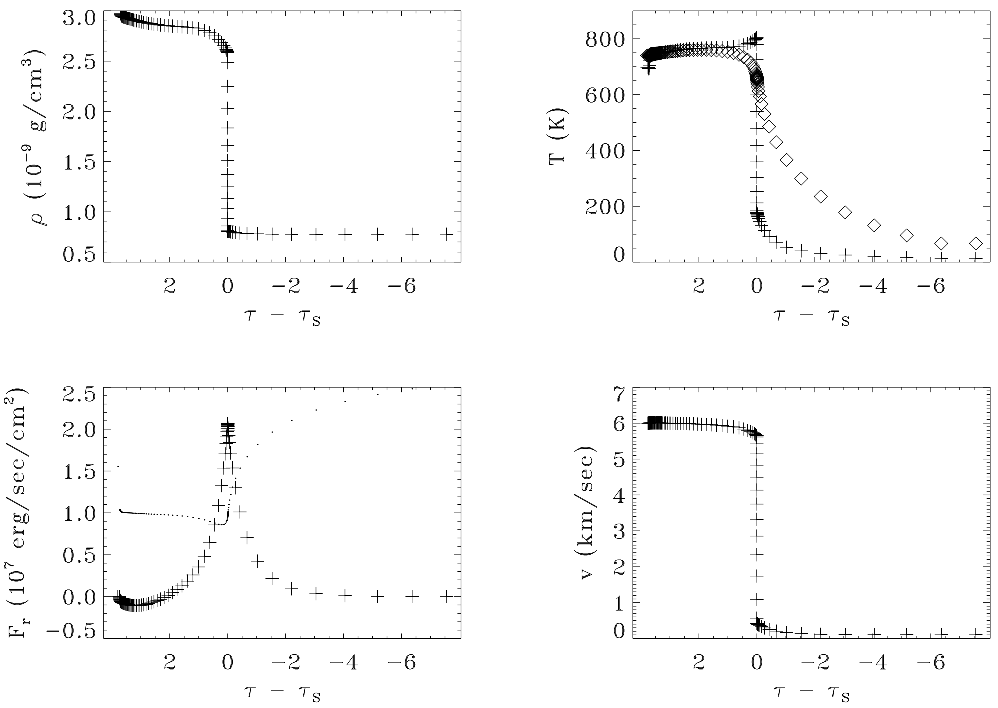

Fig. 17 (Subcritical shock): snap shots of the density, gas (+) and radiative (◇) temperature, radiative flux, and gas velocity as functions of the optical depth τ relative to the optical depth of the shock τ_s at half piston crossing time; overlayed over the flux plot is three times the Eddington factor ($\cdots$).

A non-equilibrium diffusion analysis, *cf.* Zel'dovich & Raizer, demonstrates that the density, gas pressure, radiative flux and energy all decrease upstream depend exponentially on the optical depth away from the shock:

$$\rho(\tau) \propto p(\tau) \propto F(\tau) \propto E(\tau) \propto e^{-\sqrt{3}|\tau-\tau_s|} \tag{38}$$

One consequence is that the radiative temperature must decrease slower than the gas temperature. This functional dependency on the relative optical depth holds also downstream for the flux and the gas temperature. The maximum flux is determined by the postshock temperature $T_2 : F_s \approx \frac{1}{2\sqrt{3}} a_r c T_2^4$. The analytical values differ a factor less than 2 from the actual numerical data. The behavior of our simulation agrees quite well with the analytical estimates, and the existing deviations can be explained by the use of variable Eddington factors.

4.3.2. Supercritical shock

The piston speed is 20 *km/sec*. Figure 18 shows the radiating shock while it propagates across the shell. The temperatures in the regions immediately ahead of and trailing the shock front are equal. Therefore this run is classified as a supercritical shock.

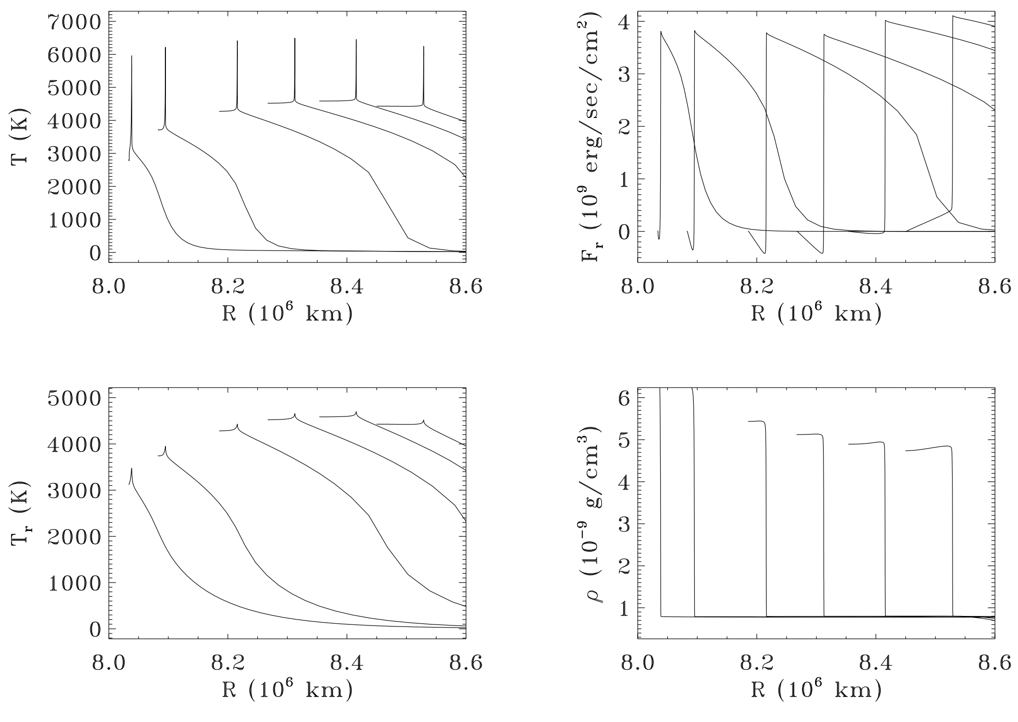

Fig. 18 (Supercritical shock): evolution of the gas and radiative temperature, the radiative flux, and the velocity profiles while a piston of speed 20 km/sec pushes the left boundary towards right.

Its characteristic features are again a strong overshoot of the gas temperature, this time a highly asymmetric flux profile, and an extended radiative precursor whose head is out of equilibrium with the gas. In contrast to the subcritical case the immediate surroundings of the shock satisfy the condition of radiative equilibrium. The temperature overshoot itself is out of equilibrium and its width is narrower than the unit mean free path of the photons. This implies that the radiation flow from this feature cannot be treated correctly by the diffusion approximation. In figure 24 the density, gas and radiative temperature, flux and Eddington factor (scaled so that 1 corresponds to $f_E = \frac{1}{3}$), and velocity are plotted in dependency on the optical depth away from the front, $\tau - \tau_s$, at one quarter piston crossing time ($t = 8,541\ sec$).

A non-equilibrium diffusion analysis according to Zel'dovich & Raizer predicts again that the radiative flux and radiative energy decline exponentially and so does the gas temperature in the upstream part of the precursor that is out of equilibrium. In the equilibrium region around the shock one finds for the gas temperature a dependency on the optical depth away from the front like

$$T(\tau) \propto \sqrt[3]{1 + \frac{3\sqrt{3}}{4}|\tau - \tau_s|} \tag{39}$$

There is also an estimate for the maximum flux which is not as accurate as for the subcritical case. Radiative equilibrium is well established within $(\tau - \tau_s) < -5$ aside of the shock front itself. Density, flux, and velocity undergo jumps from the up- to the downstream regions. Our numerical results reflect the analytical predictions. Because the analytical results are not as reliable as in the previous case a close comparison does not give good results despite the fact we actually have $f_E = \frac{1}{3}$.

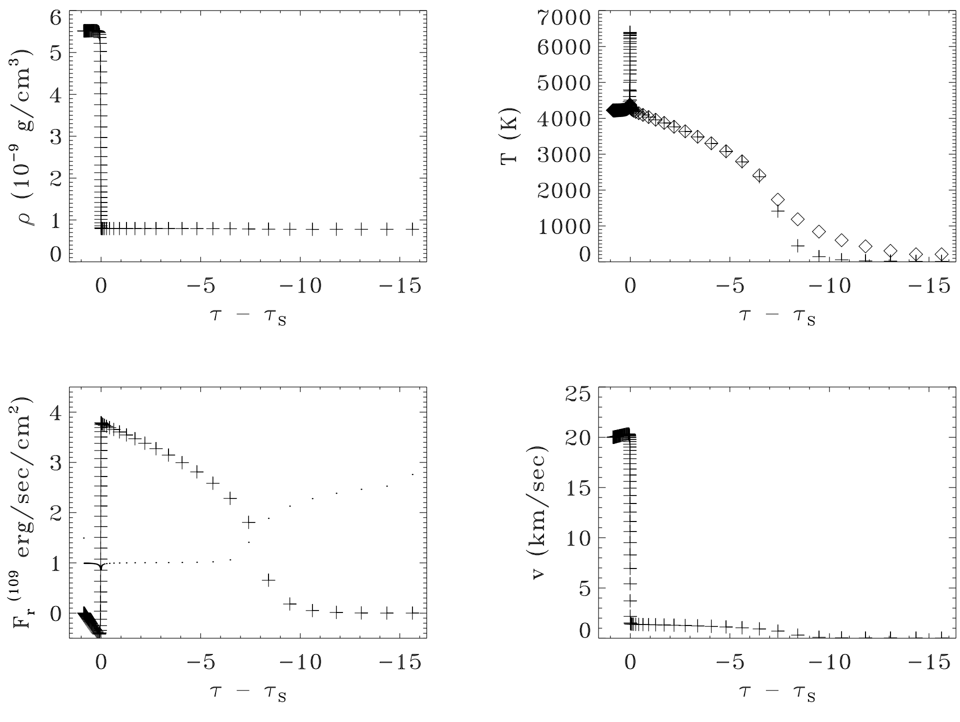

Fig. 19 (Supercritical shock): snap shots of the density, gas (+) and radiative (◇) temperature, radiative flux, and gas velocity as functions of the optical depth τ relative to the optical depth of the shock τ_s at quater piston crossing time; overlayed over the flux plot is three times the Eddington factor $(\cdots)$.

The spike in the gas temperature is prominent and very narrow. Its width is given by $(\rho\chi_e)^{-1} = 3,210\ km$. This is much larger than the rezoning limitation of $\ell \approx 80\ km$ imposed by the artificial shock width. In figure 25 on the right gas (+) and radiative (◇) temperature are plotted in the vicinity of the shock front. Their dependency in the relative optical depth is almost independent on time. The spike exists clearly only for the gas temperature while the radiative temperature varies smoothly. The spike is optically thin and hence practically transparent to the radiation (although the actual location is mostly at large optical depths). Note that there are many (around 25) grid points in this region, each zone with an optical depth of at most 5×10^{-3}. The spike is therefore numerically well represented and represents the physical, in particular radiative, properties correctly.

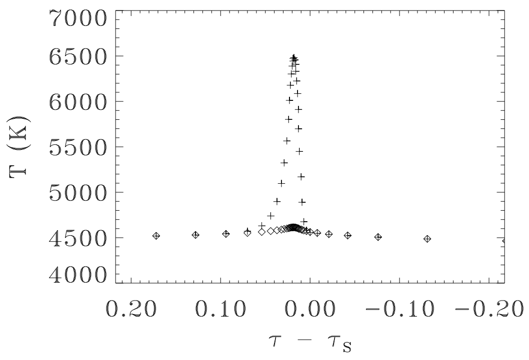

Fig. 20: Temperature spike of supercritical shock

4.3.3. Radiative blast

We now consider a shell stretching from an inner radius $R_i = 10^7\ km$ to an outer radius of $R_o = 10^8\ km$ containing a mass of 0.16 $M_\odot$. Instead of a constant density profile we assume a power law atmosphere:

$$\rho(r) = 10^{-6} \left(\frac{R_i}{r}\right)^7 g/cm^3 \tag{40}$$

The gas is purely absorptive and the mean opacity is taken to be constant and equal to the Thomson free electron scattering opacity (hence we imply the gas to be completely ionized hydrogen). The adiabatic index is $\gamma = \frac{5}{3}$. The sphere is illuminated by a central light source with a luminosity $\mathcal{L} = 10^{34}\ ergs/sec$. We obtain a self-consistent temperature profile for the initial model by relaxating the sphere's luminosity to this value using the full transport scheme, *cf.* the discission of radiative heating.

At time $t = 0$ we deposit a large amount of energy inside the sphere (corresponding to a central temperature of $10^9\ K$). This sets off a radiative blast wave (differing from the Sedov-Taylor blast wave by the fact that now the effects of radiation are included). Its evolution is followed employing the adaptive grid. As grid parameters we choose the mass, density, and radiative energy in logarithmic and the velocity u (1000 km/sec) in linear scaling, together with $\alpha = 1.5$, $\tau = 10^{-20}$, and $\theta = 1$. The shock width is $\ell_1 = 10^{-4}$. After initiating the blast wave it reaches the surface in 700 time steps.

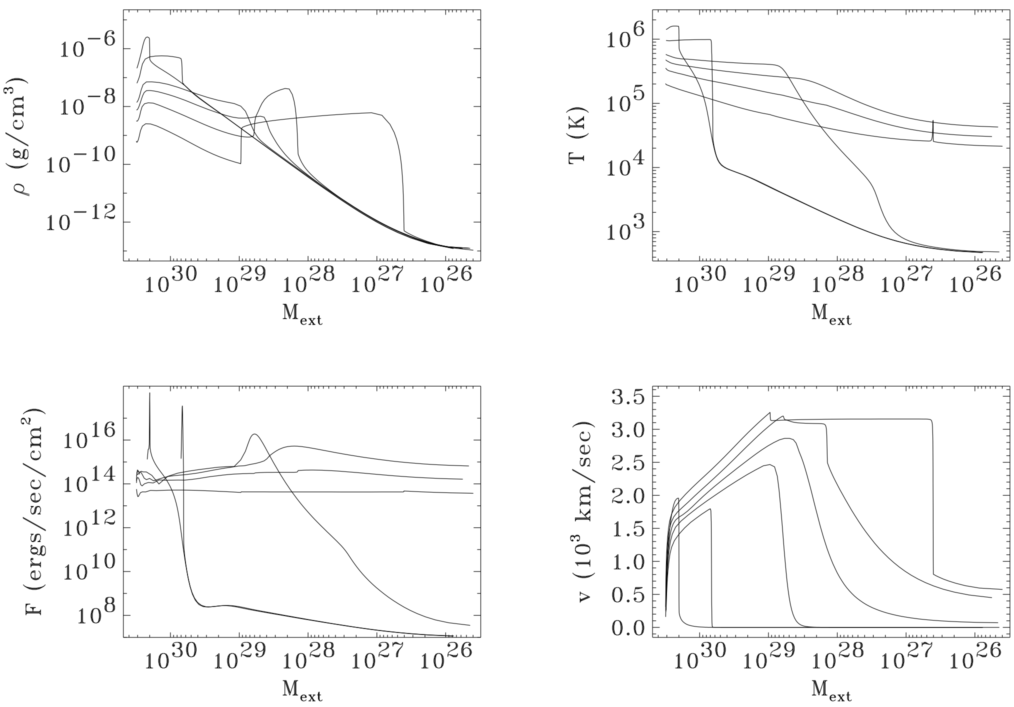

Fig. 21 (Radiative blast): snap shots of the density, gas temperature, radiative flux, and gas velocity as functions of the exterior mass log M_{ext} at six different times t $\in$ (437, 2162, 7134, 10329, 15562, 29099) sec; the corresponding optical depths of the shock front are $\tau \in (3.2\times10^4$, 6.25×10^3, 184, 61.5, 15.9, 0.17).

In figure 21 the evolution of the gas sphere is depicted at six different times. Initially the shock moves down the density and temperature gradient. There is a very prominent flux peak and the shock profiles for density, temperature and velocity are sharp. The shock looks like an adiabatic one. In time the radiation preheats an increasing region ahead of it. When the shock has penetrated to an optical depth of about 200 (which occurs at time $t \approx 7000$ sec) this radiative precursor has reached the surface. The surface luminosity rises very fast and reaches its maximum at about $t = 1.13 \times 10^4$ sec, see figure 22. The gas and radiative temperatures are out of equilibrium at the head of the precursor. The heating induces a quasi-isothermal wind in the outer shell and the gas equilibrates again. Before reaching an optical depth of 60 the shock has dissipated through the radiative processes. The shocked gas, however, maintains its momentum and begins a "snow plow" phase where it sweeps up wind material. The surface luminosity declines and an almost constant flux profile becomes established. The sphere begins to cool off. Behind the "snow plow" a very dense shell is formed which is well established by $t \approx 1.5 \times 10^4$ sec at optical depth $\tau = 16$. While the plow steepens up at its head to a strong supercritical shock (with the typical temperature spike) another, reverse shock forms at its tail. It propagates slowly into the homologously expanding inner regions. The dense shell expands rapidly and moves at nearly the shock speed outwards. Through the radiation the gas keeps cooling down, and, since the almost constant flux level decreases, the surface luminosity keeps dropping.

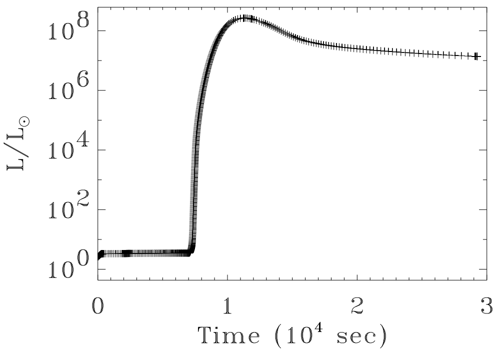

Fig. 22: surface luminosity as a function of time; the + signs mark individual time steps.

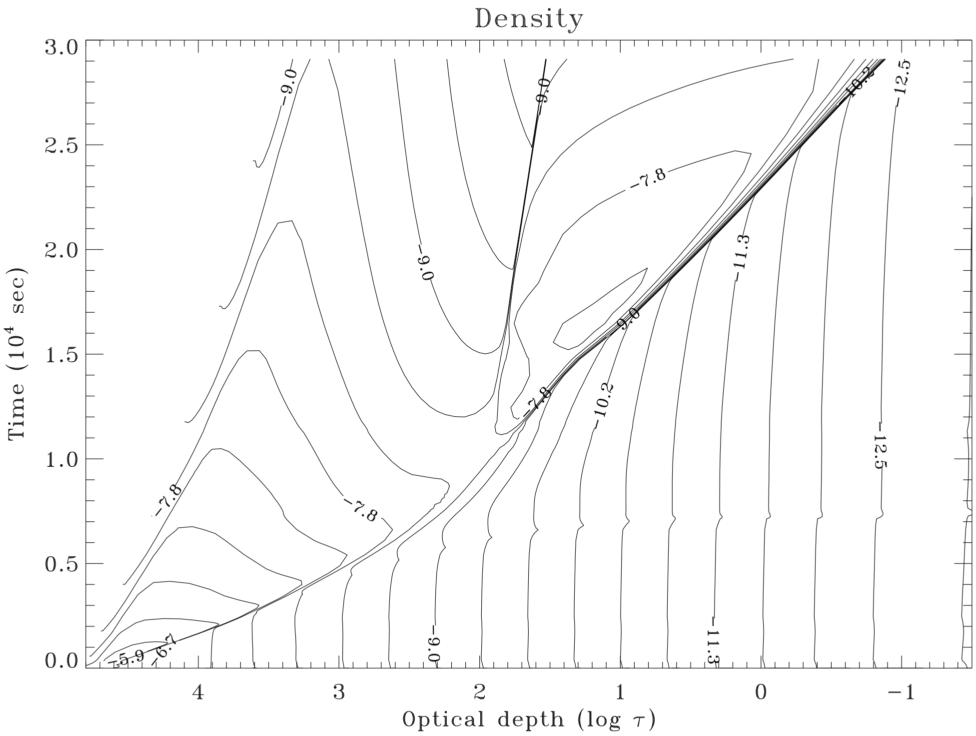

Fig. 23 (Radiative blast): optical depth-time diagram of the logarithmic density in g/cm^3.

The evolution of the radiative blast simulation can be illustrated via "optical depth-time diagrams" of the density, velocity, and temperature (figures 23 – 25). One can recognize the adiabatic shock during the initial phase up to several 1000 *sec*. While it dissipates through radiative losses the radiative precursor surfaces at about 10^4 *sec* and the luminosity there breaks out. The shocked regions plow into the isothermal wind while the gas keeps cooling off. A new supercritical shock is born and runs fast towards the surface. Simultaneously a reverse adiabatic shock forms. It moves into the inner regions which already undergo a homologous expansion and a high density shell at a constant speed is created.

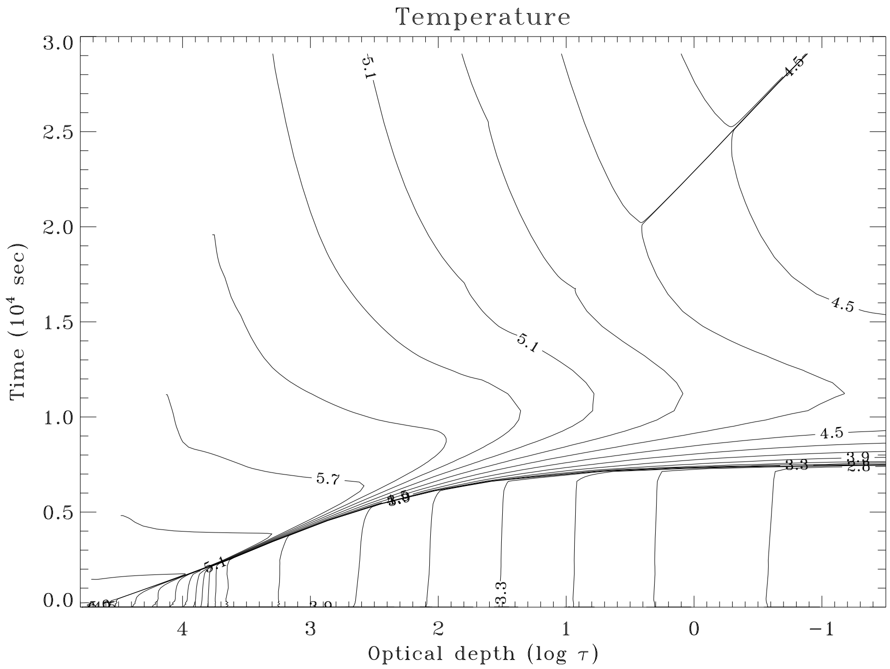

Fig. 24 (Radiative blast): optical depth-time diagram of the velocity in 1000 km/sec.

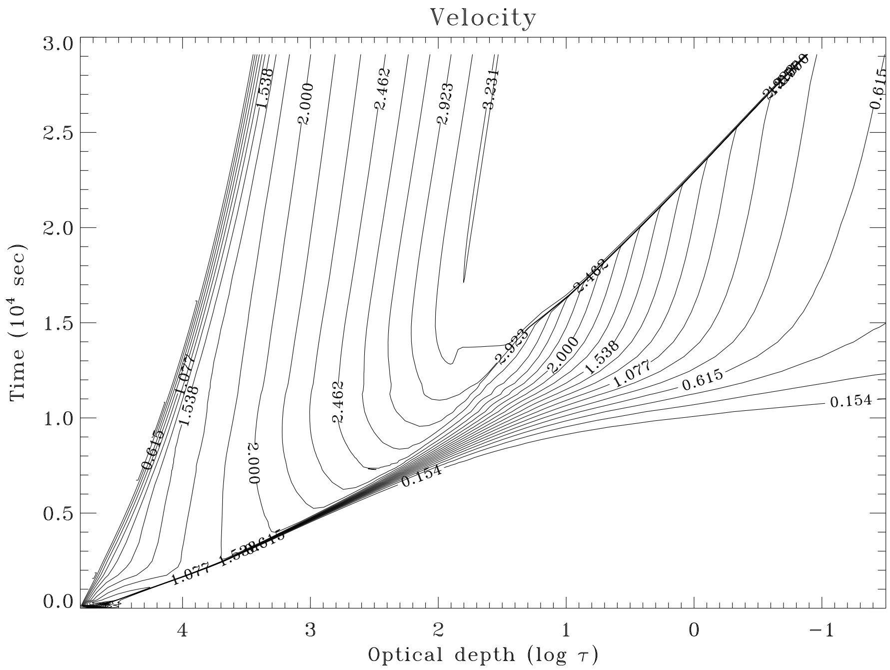

Fig. 25 (Radiative blast): optical depth-time diagram of the logarithmic gas temperature in K.

The grid motion is depicted in figure 25 in which every fourth zone is plotted as a function of optical depth and time. After a very short relaxation period the grid points begin to zoom into the forming shock, $t \approx 2000$ *sec*. They actually lock into the radiative precursor until it surfaces at $t \approx 7000$ *sec*. The grid then rezones quickly to resolve a new shock system that forms around $t \approx 10^4$ *sec*. It tracks a reverse shock and follows a forward shock all the way to the surface.

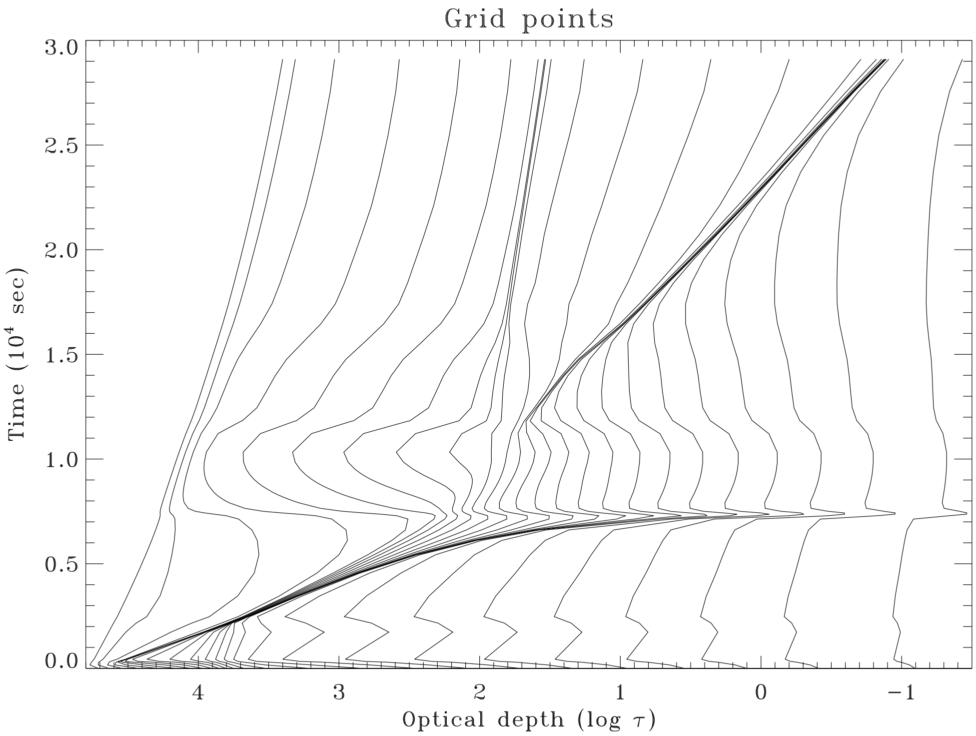

Fig. 26 (Radiative blast): optical depth-time diagram of the grid point motion; every fourth zone is shown.

5. Conclusions

We have presented a state-of-the-art computational tool for solving the one dimensional equations of radiation hydrodynamics. In a series of test problems we have demonstrated its powerful numerical technique and demonstrated its versatility and reliability. The adaptive grid has been proven to be superior over conventional, *i.e.,* Lagrangean and Eulerian, schemes because it provides an intelligent way to detect, resolve and track the relevant nonlinear features in the flow. This not only guarantees solutions of very high quality, but also generates them faster or makes them possible for the first time.

In the following short discussion we attempt to relate our test problems to real problems: One good example for a hydrodynamical shock is a nuclear fireball. It starts off as an r-front, then evolves to a d-front with a preceding shock. This is a hard problem for a fixed grid (Lagrangean) code because the thickness of the ionization region is only a few mm, but the code must propagate it over km distances. Dealing with these length scales and keeping the ionization zone resolved is a perfect problem for an implicit adaptive grid code. From a physical point of view the hydrodynamical shock can be so strong that it radiates as a result of the deposition of kinetic energy into the shocked material. Our "light bulb" tests could be related to some brief phases of stellar evolution where a star just ignites its thermonuclear burning, or where a star taps into a new thermonuclear source, or where a star experiences a runaway like the helium flash at the tip of the giant branch. The sudden rise in available energy should drive a very steep d-front out. Both the shock and the ionization front would require adaptive grid resolution. Clearly, supernovae give opportunities for very strong radiating shocks. These, however, are relatively easy to resolve because the radiation is so strong that it disperses the shock, and all physical variables are continuous across the front. On the other hand, variable stars like cepheids are an ideal problem for an adaptive grid code. There the ionization region is a d-front inside the star. It is very steep because of the rapid variation of the hydrogen opacity with temperature. As it burns out the d-front briefly converts into an r-front. Then the primary shock runs out. We conjecture that it is supercritical but this needs yet to be demonstrated by a high-resolution computation. Other possible applications of an adaptive grid code are instances where one is interested in thermonuclear burn which leaves behind (or builds up) steep composition gradients. Finally we suggest ICF pellet problems as prime candidates for adaptive grids. The radiation that burns in is extremly hot, so that the front is steep and far from equilibrium.

TITAN is already available as a community code. For this reason we designed it in a modular fashion to allow for a large variety of applications. The code itself is written in a comprehensible and user friendly manner. A user's guide together with an in-depth reference manual is provided. We took great care in testing and debugging TITAN as far as humanly possible to render it a realible research tool. In the first distribution phase we release the code to a "friendly user's group" in order to test its impact on current research topics. In the second distribution phase we will make it available to the general public.

We are currently working on various extensions of the existing code. One immediate step is to implement some models for time dependent turbulent convection which often play an important role in the transport of energy. Another path we intend to follow is to incorporate NLTE physics to allow the computations of spectral lines, and the formulation of a self-consistent multigroup approach to the radiative transport.

Acknowledgements. D.M. wishes to thank the National Center for Supercomputer Applications and the National Solar Observatory for their contributions to his sabbatical leave support during the academic year 1992-1993. M.G. thanks C. Keller and the IGPP at Los Alamos National Laboratory for their warm hospitality during which part of this work has been accomplished. Both authors would like to thank L. Ensman for many valuable discussions on benchmarking a radiation hydrodynamics code. We are grateful to P. Whalen for insisting on computing some challenging hydrodynamics problems. Finally, we thank K.-H. Winkler for introducing us to, and teaching us about, adaptive-grid

techniques in radiation hydrodynamics.

This work has been supported in part by National Science Foundation grants AST-8914143 and AST-920113, National Aeronautics and Space Administration grant 90-NASA-M-1665, and research funds made available by the University of Illinois.

6. References

1. R. Courant and K. O. Friedrichs. "Supersonic Flow and Shock Waves" Interscience Publishers, New York, 1969.
2. A. N. Cox, R. G. Deupree, and M. Gehmeyr. *Physica D*, **60**, p. 139, 1992.
3. E. A. Dorfi and L. O'C. Drury. *Journal of Computational Physics*, **69**, p. 175, 1987.
4. L. Ensman. *Ph. D. Thesis*, University of California at Santa Cruz, 1991.
5. L. G. Henyey, J. E. Forbes and N. L. Gould. *The Astrophysical Journal*, **139**, p. 306, 1964.
6. L. D. Landau and E. M. Lifshitz. "Fluid Mechanics" Pergamon Press, Oxford, 1987.
7. D. Mihalas and B. W. Mihalas. "Foundations of Radiation Hydrodynamics" Oxford University Press, Oxford, 1984.
8. W. A. Mulder and B. van Leer. *Journal of Computational Physics*, **59**, p. 232, 1985.
9. W. F. Noh. *Journal of Computational Physics*, **72**, p. 78, 1987.
10. G. A. Sod. *Journal of Computational Physics*, **27**, p. 1, 1978.
11. W. M. Tscharnuter and K.-H. A. Winkler. *Comput. Phys. Commun.*, **18**, p. 171, 1979.
12. K.-H. A. Winkler and M. L. Norman. *In:* "Astrophysical Radiation Hydrodynamics" (K.-H.A. Winkler and M.N. Norman, eds.), p. 71, D. Reidel Publisher, Dordrecht, 1986.
13. K.-H. A. Winkler, M. L. Norman, and D. Mihalas. *Journal of Quantitative Spectroscopy and Radiative Transfer* **31**, p. 121, 1984.
14. P. R. Woodward and P. Collela. *Journal of Computational Physics*, **54**, p. 115, 1983.

15. Ya. B. Zel'dovich and Yu. P. Raizer. "Physics of Shock Waves and High Temperature Hydrodynamic Phenomena" Academic Press, New York, 1966.